

CHAPTER 4

EXPERIMENTAL INVESTIGATION



4.1 Full-Scale Testing

An experimental program of full-scale testing was carried out at Chulalongkorn University to verify the numerical results of link slabs under the action of mid-span loading in the previous chapter. The behavior of link slabs under mid-span loading was observed for crack distribution, crack width, stress in reinforcing steel, load-deflection relationships, failure modes and ultimate strength through full-scale testing considering variable lengths of lap reinforcement.

4.1.1 Test Program and Test Set-up

Only the mid-span loading was simulated and the length of the lap reinforcement was the key parameter in the test. Three link slab specimens, with a thickness of 200 mm, span length of 2000 mm and width of 1000 mm were tested as shown in test program (Table 4.1). The characteristic compressive strength of concrete was 300 kg/cm^2 and the yield strength of reinforcing steel was 4000 kg/cm^2 . Table 4.2 shows actual dimensions of test specimens with their corresponding concrete and reinforcement steel strength.

The link slab specimens were prepared in the full-scale testing laboratory with the supports that were fixed to the laboratory floor to simulate fixed-end condition.

The quantities that were measured in the test included strain in reinforcement, deflections, support movement, crack distribution, crack width, corresponding load and ultimate load capacity. Electrical resistance strain gauges with a length of 5 mm were fixed across the mid and edge sections of the link slabs at both top and bottom reinforcements in order to measure the tensile and compressive strains. Out-of-plane deflections at four points along the mid-section, at one-sixth span and at both supports were measured by using linear variable deflection transducers (LVDT) as shown in Fig. 4.1.

Three link slab specimens were tested to failure under a central point loading of an actuator of 100 ton capacity. To represent the AASHTO HS20-44 wheel load, the load was transmitted over a rectangular steel plate of 500 mm x 200 mm x 20 mm (AASHTO, 2002). The test set-up is shown in Fig. 4.1. The test was performed right after the concrete reached the specified strength, and the LVDT, load cell and strain gauge signals were the input for the computerized data acquisition system.

The specimens were gradually loaded up to 1 ton and the load was subsequently released to ensure that the loading edges remained in proper contact with the specimens. Thereafter, the specimens were subjected to two cyclic loads. First, they were cyclically loaded to 20 tons with a 1 ton increment to observe cracking load and tension stiffening behavior before and after cracking. A cyclic load of 9.3 tons, which represents the factored load for the AASHTO HS20-44 wheel load (plus 30% impact), was then applied 5 times to observe the link slab behavior under service level. Thereafter, they were loaded with a 5 ton increment until a substantial increase in displacement was observed to establish a base line curve and to detect specified crack widths. Finally, the specimens were loaded until they failed.

4.1.2 Test Results

The first cracks of both LS_S and LS_F slabs were observed simultaneously at the mid-span and near the supports, whereas for the LS_H slab, the first crack was found at the mid-span. Cracking loads for specified crack width obtained from the experiment are summarized in Table 4.3. It is also observed that the base line curves of each loading cycle (from 0 to 9.3 ton) are similar for all lengths of lap reinforcement. The reinforcing steel did not yield before shear failure took place.

The LS_H slab acts as a cantilever slab with horizontal compression at the upper part of the mid-span section. Before failure, it had a horizontal crack at the uppermost side of the mid-span section due to the compressive force, and an inclined crack at the support ends. These two cracks were the main causes of the failure.

For the LS_S slab, it acts as a continuous slab until the flexural shear crack occurs because the positive moment cannot be fully developed due to the insufficient double lap reinforcement. The weak section is at the location of lap reinforcement, the failure cracking plane is then close to the loading pad and lap reinforcement. In the LS_F slab, the positive moment can be fully developed due to double reinforcement at

the mid-span section. In addition, the failure crack has an axis of symmetry at a point half-way between the mid-span and end-span and the horizontal cracks are clearly observed at both end-span and mid-span sections. Failure occurs due to either crushing of the reduced concrete section at the bottom of the end-span and the top of the mid-span in all slabs, called shear compression failure, or crack splitting of the concrete cover along the reinforcing steel in the LS_S and LS_F slabs.

The results also indicate that the inclined tie angle and the position of failure plane for each reinforcement detail are different. In the LS_S and LS_F slabs, the angle is approximately 30 degrees, which is an angle that usually occurs in a prismatic beam. However, the failure plane of the LS_F slab is located at the quarter-span of the specimen but that of LS_S slab is close to the mid-span. In addition, the LS_H slab shows the inclined angles at the cracking planes of 10, 20, and 30 degrees at mid, quarter and end of the span respectively. Because the applied loading is not a line load, the crack across the section is not uniform. It is very difficult to detect the first inclined crack since it occurs inside the slab and the inclined crack angle observed at the side surface is just lower than that which occurs inside.

The shear strength of reinforced concrete slabs or beams without shear reinforcement provided by uncracked concrete sections, aggregate interlock and dowel bars was developed in ACI318-05 (2005) which is given by:

$$V_c = \left(\sqrt{f'_c} + 120 \rho_w \frac{V_u d}{M_u} \right) \frac{b_w d}{7} \leq 0.3 \sqrt{f'_c} b_w d \quad (4.1)$$

where $\rho_w = A_s / b_w d$, A_s is area of non-prestressed tension reinforcement, d is effective depth of section, b_w is width of the beam web. From the test results, failure loads of the LS_H and LS_F slabs are about 25% higher than shear strength due to beam behavior, whereas the failure load of the LS_S slab is about 40% higher because of the arch behavior. The lateral restrained link slab exhibits internal arching action that strengthens the link slab through the confinement provided by a complex three-dimensional membrane stress around loaded area. As a result, the slab fails due to shear rather than flexure.

The deflections of the test specimen were measured at four equally-spaced points from the support to the mid-span. These values with the symmetrical assumption can be used to predict the deflected curves, the inflection points and curvatures of the slab provided that the deflected curve is approximated by a 4th-order

parabola. It is found that the inflection points for the LS_F, LS_S and LS_H specimens occur at $0.18L$, $0.22L$ and $0.27L$ from the support respectively where L is the span length of the link slab. The inflection points determined from finite element analysis are found at $0.22L$, $0.23L$ and $0.25L$ respectively for the LS_F, LS_S and LS_H slabs. At the same load, curvatures at the end-span and mid-span of the LS_H slab are higher than those of the LS_F and LS_S slabs. These results confirm that the locations of inflection points and curvatures depend significantly on the length of lap reinforcement. Since the reinforcement for the positive bending moment in the LS_F slab is heavier than the negative moment reinforcement, the inflection point then moves toward the supports. On the contrary, the reinforcement at the mid-span section of the LS_H slab cannot carry the bending moment since the slab behaves after cracking as a cantilever slab, the inflection point then moves to the mid-span. Therefore, the LS_H slab yields the largest deflection followed by the LS_S and LS_F slabs respectively. The behavior of the LS_S slab is in between the LS_H and LS_F slabs, i.e. it behaves like a semi-continuous slab.

4.1.3 Comparison between Finite Element Analysis and Test Results

Failure loads and corresponding mid-span deflections from the full-scale test are presented in Table 4.3 and they are compared with the finite element solutions. Comparisons of tensile stresses in reinforcing steel at the end-span (top reinforcement) and the mid-span (bottom reinforcement) for all reinforcement details between finite element and experimental results are also shown in Fig. 4.2. Both results agree well on the top reinforcement stresses at the end-span for all reinforcement details because the locations of strain gauges were close to the estimated crack positions. However, the stresses in the bottom reinforcement at mid-span from FEM and the experiment are quite different due to the discrepancy in the locations of strain gauges and random cracks as well as the deformed curve of the experiments under the loading pad.

Numerical results presented in Fig. 4.2 also indicate that the stresses in reinforcement at the mid-depth across the saw cut obtained from the test of LS_H specimen is much higher than the finite element results. The reason for this inconsistency is that the depth of the compression zone at the mid-span section from the finite element analysis is about twice as larger as that shown in the experiment. Therefore, the mid-span section of the LS_H slab from the present FEM is stiffer, and

a different finite element model that can simulate a very large concentrated crack is recommended for the analysis of a link slab with no lap reinforcement.

Figure 4.3 presents a comparison between the maximum crack widths estimated from reinforcement stresses due to finite element analysis and those measured in the experiment. The maximum surface crack width at each loading step from finite element analysis is estimated by using the AASHTO (2002) and ACI Building Code (2005), which is given by

$$w_{cr} = 0.000076\beta f_s \sqrt[3]{d_c A} \quad (4.2)$$

where w_{cr} is the crack width in inch; β is the ratio between the distance from the extreme tension fiber to the neutral axis, and the distance from the centroid of the main reinforcement to the neutral axis, and it can be taken as 2 (Caner, 1996); f_s is the rebar stress in ksi; and d_c is concrete cover from the extreme tension fiber to the centroid of the nearest rebar level. In addition, A is the effective area per reinforcing bar in in^2 . It can be seen from Fig. 4.3 that good agreements between both results are obtained for the LS_S and LS_F slabs. The maximum crack width measured from the LS_H slab is different from that estimated from finite element analysis due to the discrepancy in level of the neutral axis at the mid-span section discussed in the foregoing paragraph. Nevertheless, the difference between the maximum crack widths in the LS_H slab estimated from FEM and the experiment is acceptable for practical applications. Therefore, the finite element model presented in this study can be used to develop the serviceability limit state for a link slab. The advantage of making a saw cut in the LS_H slab is to generate a concentrated crack in one location, which can be easily repaired, instead of several cracks. The drawback is that the variation of stress in reinforcement across the saw cut is so high that it has to be carefully monitored to ensure that the stress variation is within the acceptable limit to prevent fatigue failure.

The crack distribution and the direction of failure cracking planes from the experiment and finite element analysis are presented in Figs. 4.5(a) and 4.5(b) respectively. Those numerical results can be used to verify the inclined angle of a tie in the strut-and-tie model, in which the angle of 60 degrees for a flexural member without transverse reinforcement is proposed (Reineck, 1991). The angle of the inclined tie is perpendicular to the direction of the cracking plane. A good agreement between the two results is observed for all specimens as shown in Fig. 4.4.

A comparison of the load-deflection curves in Fig. 4.5 indicates a close agreement between the experiment and finite element results for the LS_S and LS_F slabs. However for the LS_H slab, in addition to the different depth of the compression zone at the mid-span section between the two results as previously discussed, the tension stiffening is partially lost resulting in lower stiffness in the test specimen than the finite element model when the load is sustained or applied repeatedly. This is due to the fact that the bending moment cannot be redistributed in a determinate structure after a crack is formed at the mid-span of the LS_H slab.

In the case of a beam with fix-ended supports subjected to a central point load, the effective moment of inertia is calculated from the following equation:

$$EI_{\text{exp}} = \frac{PL^3}{192\Delta} \quad (4.3)$$

where P and Δ denote the magnitude of applied loading and the mid-span deflection respectively. For a given load-deflection diagram, the effective moment of inertia from either finite element or experiment results can be calculated by using Eq.(4.3). The effective moment of inertia can also be obtained from Branson formula (1965) for given values of weight factors and the exponent m . The appropriate values of weight factors and exponent m from both FEM and experiment results are determined by using a least square method with the initial values of (0.30,0.70) and 3 respectively for weight factors and m . It was found that the difference between the effective moment of inertia computed from the last chapter, and that from Eq.(4.3) is within 10 percent. The weight factors are 0.3 and 0.7 for negative and positive bending moments respectively from the Branson formula. However, the weight factors obtained from the experimental results are (0.23, 0.77) and (0.34, 0.66) for the LS_F and LS_S slabs respectively. These values are in good agreement with the weight factors computed from finite element analysis, which are (0.22, 0.78) and (0.31, 0.69) for the LS_F and LS_S slabs respectively. The weight factor for negative bending moment of the LS_F slab is less than that of the LS_S slab since the length of lap reinforcement at the mid-span of the LS_F slab is much longer. As a result, the mid-span section of the LS_F slab is stiffer and the negative bending moment zone is then shorter. Note that the LS_H slab does not follow the assumption of the Branson-based formula since this slab behaves like a cantilever slab.

The value of the exponent m was originally proposed to be 3 by Branson (1965). Al-Zaid, et al. (1991) later suggested that this value should be 2.8, 2.3 and 1.8

for a beam under uniformly distributed loading, third-point loading and mid-span concentrated loading respectively. Since the mid-span loading in this study is applied through a loading plate, which is not an actual point load, the proposed value for m then varies from 1.8 to 2.3. It was found that the optimal values of m from the experimental results were 2.5 and 2.7 for the LS_F and LS_S slabs respectively, whereas from the finite element analysis, they were 2.3 and 2.5 for the LS_F and LS_S slabs respectively. This implies that the suggested value of m between 1.8 and 3 can not be used for the LS_H slab, which has no lap reinforcement and a large crack is concentrated at the mid-span section.

The moment and curvature at the edge and mid-span where has maximum moment from strain gauge which is attached on reinforcing steel can be determined. Moment-curvature relationship is compared with section analysis and with the experimental result as shown in Fig. 4.6. It is shown that in each specimen that reinforcing steel did not yield, however, stress in reinforcing steel in LS_H is more than in LS_S and LS_F respectively. Maximum stresses in reinforcing steel in LS_H, LS_S and LS_F are about 3400 ksc, 3100 ksc, and 2000 ksc respectively. They are from negative moment at the edge of the slab. They show that in each reinforcing detailing they have a different moment distribution. LS_H acts as a more cantilever structure than others at the same load in which most moment is transferred to the edge. From the deflected curve, the curvatures at each point can be determined by differentiation of deflection equation. In addition, from the inflection point, the bending moment diagram can be approximated due to mid-span loading. The moment-curvature relationship from the deflected curve is also shown in Fig. 4.6. This moment-curvature is not quite correct because of shear deformation and data accuracy, however, it can approximate the sectional behavior.

4.2 On-Site Monitoring

The behavior of an elevated highway structure with link slabs was observed for the end movements of each girder through on-site monitoring. The consideration of the site selection are straight route, no elevation, having buildings or a safe place to keep instruments, having link slabs as the structure that makes a continuous deck with the equally span length, access to the instruments, having different types of

elastomeric bearing pad in different piers and having the same substructure. The elevated highway site where can be monitored following the above consideration is Ramindra-Atnarong expressway.

Ramindra-Atnarong expressway project is a 6-laned elevated structure (3 lanes in each direction) which is 18.7 km in length and located in a north-south direction in Bangkok. The typical superstructure system consists of a simply supported I-girder of typical 30 m in length, in-situ reinforced concrete slabs with 8 cm thickness of asphalt, continuous slabs 180 m in length with link slabs between each spanned girders, reinforced elastomeric bearing pads made of natural rubber and steel laminated plates without mechanical anchorage, and expansion joints (metallic and elastomeric expansion device) between the continuous slabs.

The typical substructure system is a reinforced concrete inverted T-beam supported by a single pier fixed with the pile cap which is designed in accordance with the girders and their location along its length. The chosen monitoring site is the Ramindra-At Narong expressway between pier number 11+591.500 and 11+771.500 which is a 6 spans continuous deck, 30 meter-span length in each span, 9 centimeter-maximum elevation and 200 meter radius. This site is the best one to follow the above consideration which is the most straight route, with less elevation, having a building to keep instruments near the site, accessibility of measurement and having link slabs as the structure that make a continuous deck with the equal span length.

4.2.1 Instrument Installation

The overview of the highway site and the instrument installation are shown in Figs. 4.7 – 4.8. Two different levels of longitudinal movement and one vertical movement of end girder at each pier are measured by using linear variable deflection transducers (LVDT). The monitoring points are on only 3 piers along the route and each pier has 3 LVDTs because of site limitations. Two horizontal LVDTs installed at different levels (50 centimeters) at each pier (HT#1,2,3 and HB#1,2,3) measured the longitudinal movement and were calculated to end rotation by dividing the differential longitudinal movement by the length between two horizontal LVDTs. One vertical LVDT at the center of elastomeric bearing on each pier (V#1,2,3) measured the vertical movement due to elastomeric bearing that its pin must be allowed free horizontal movement to prevent the wrong data and instrument damage. During

monitoring, LVDT signals were input to a computerized data acquisition system. The dial gauge installation was also done at the expansion joint pier for rechecking the LVDT signal because this position is easy to access by humans and this position has the highest longitudinal movement. The ambient temperature data were collected from the Don-Muang international airport station which is closest to the monitoring site of meteorological department because of some restriction.

4.2.2 Monitoring Result

From the monitoring results and the ambient temperature data, it can be concluded that the horizontal movement of girders is looped movement which follows the looped ambient temperature. At the free end of the continuous deck the horizontal movement was much more than other at internal span because of no restraints. The monitoring results are shown in Fig. 4.9 which are ambient temperature, each LVDT signal, and calculated end rotation. The monitoring amplitude results at each position have been related to the rotational and longitudinal movements in accordance with the interaction model in chapter 3. In addition the movement has different noise which depends on elastomeric bearing pad types.

From axial movement of each end girder, the ambient temperature affects the axial movement of girders which has a mid-span of continuous deck as the fixed point because of the elastomeric bearing pad has more horizontal stiffness at this point. So the longitudinal movement of end girders at pier 3 (LVDT no. HT#3 and HB#3) is more than that at pier 2 (LVDT no. HT#2 and HB#2) and pier 1 (LVDT no. HT#1 and HB#1) respectively as shown in Fig. 4.9.

The time period that girders were shortened or moved to the fixed point was around 5 p.m. to 9 a.m. And the duration that girders are stretched or moved out the fixed point was around 9 a.m. to 5 p.m. which is related to the time of sunlight. The maximum and minimum ambient temperature occurred at 3 – 4 p.m. and 6 – 7 a.m. The time lag between ambient temperature and structure temperature was about 2 hours. The horizontal movement due to ambient temperature from monitoring was comparable to result from analysis. The differential ambient temperature is about 10 °C and span length is about 30 m that results in 1.65 mm of horizontal movement in each side. The result from analysis with unrestraint assumption is about 55%, 70%,

40% more than the result from monitoring at the pier 1, 2, 3 respectively as shown in Fig. 4.9.

From end rotation results, the temperature gradient affects the camber and deflection of the girders. The end rotation of girders from monitoring is comparable to results from the girder model as mentioned in chapter 3. The differential temperature between the top and bottom of girders is assumed to be about 25°C that results in $0.3\text{E-}3$ to $0.7\text{E-}3$ radian of end rotation from the girder model. The result from monitoring results are in the bound of the results from girder model as shown in Fig. 4.9.

The vertical movement due to axle truck load passed through end girders and elastomeric bearing pads effect from monitoring is comparable to result from analysis. The vertical stiffness of elastomeric bearing pad is about 134, 69.4, 46.8 T/mm for type 1, 2, 3 respectively. The axle truck load is about 14 T and it has about 6 bearing pads in transverse direction of highway. The vertical movement from analysis is about $0.017 - 0.050$ mm that is similar to the result from short period monitoring ($0.01 - 0.02$ mm). The axle truck load is considered only 1 truck because this highway has a low degree of traffic. The vertical movement results were also affected by the ambient temperature.

Table 4.1 Test program

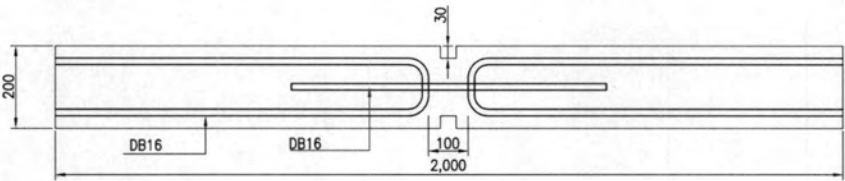
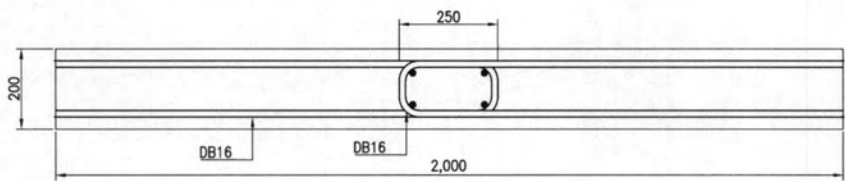
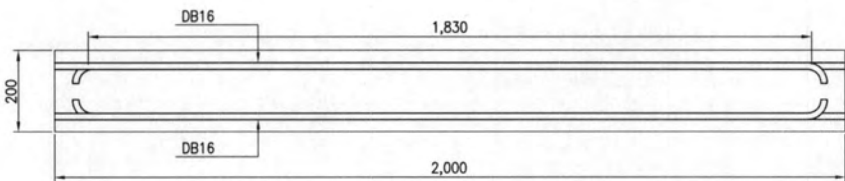
Name	Reinforcement Details
LS_H	 <p style="text-align: center;">Hinged</p>
LS_S	 <p style="text-align: center;">Semi-continuous</p>
LS_F	 <p style="text-align: center;">Fully continuous</p>

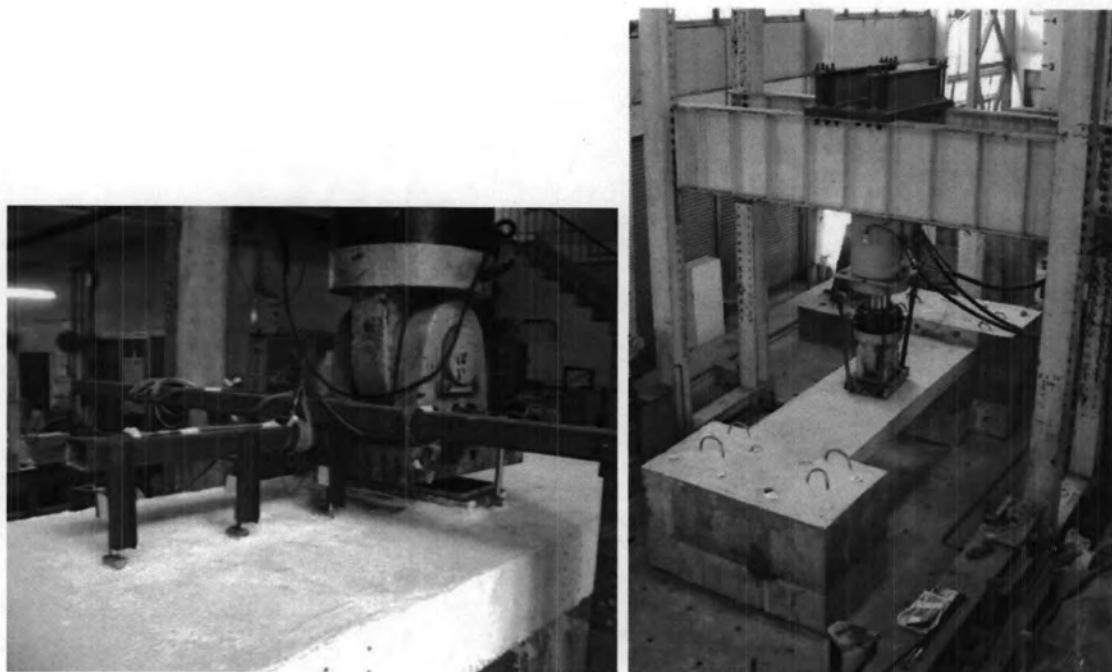
Table 4.2 Properties of test specimens

Specimen	Average thickness (mm)			Level of reinforcement (mm) upper/lower			Concrete Strength (ksc)	Reinforcing steel yield Strength (ksc)
	End1	Middle	End2	End1	Middle	End2		
LS_H	202	203	202	162/32	168/35	164/32	233	5530
LS_S	200	200	205	165/31	165/38	160/31	261	5750
LS_F	203	205	203	168/30	169/33	169/32	333	5760

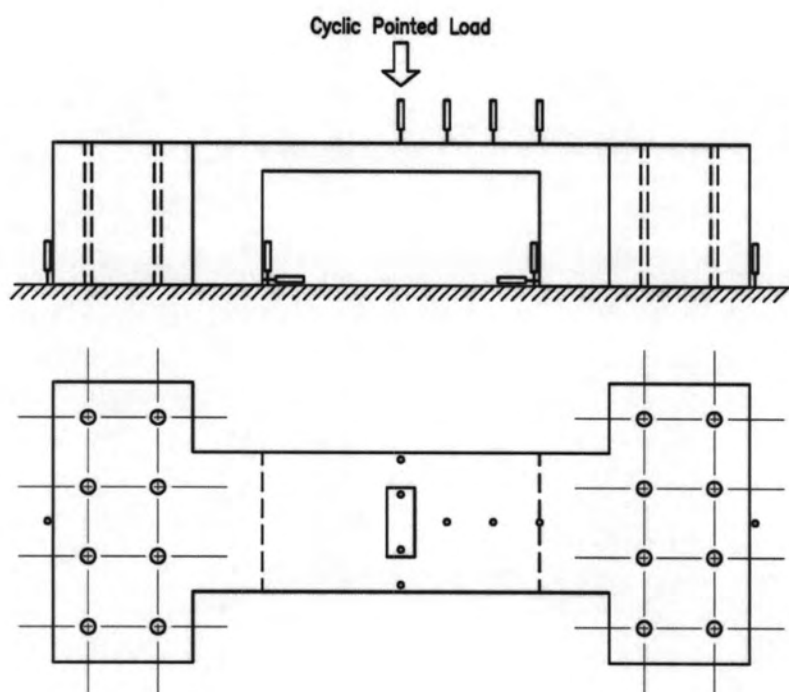
Table 4.3 Crack and failure loads

Specimen	Load at specified crack (kN)				Failure load (kN)		Maximum deflections (mm)	
	1st crack	0.2 mm	0.3 mm	0.4 mm	Experiment	FEM	Experiment	FEM
LS_H	30	60	90	150	635.9	655.2	10.89	6.86
LS_S	110	300	400	700	809.6	908.2	7.28	6.69
LS_F	120	400	700	*	777.8	824.7	3.73	4.52

* Failed prior to specified crack

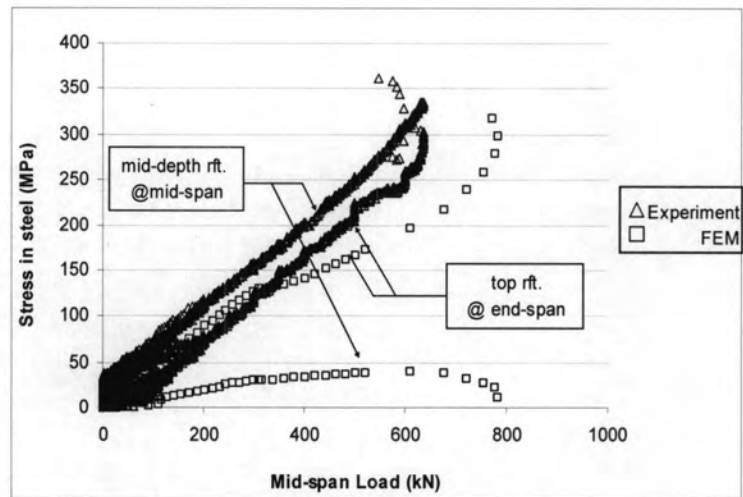


(a) Loading arrangement

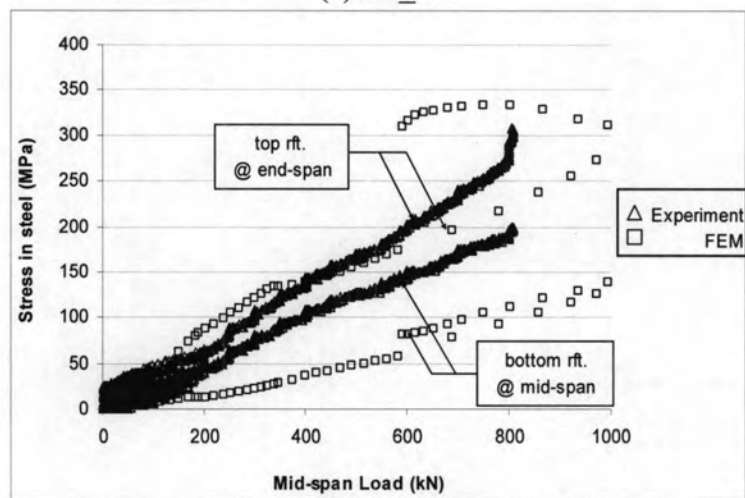


(b) LVDT position

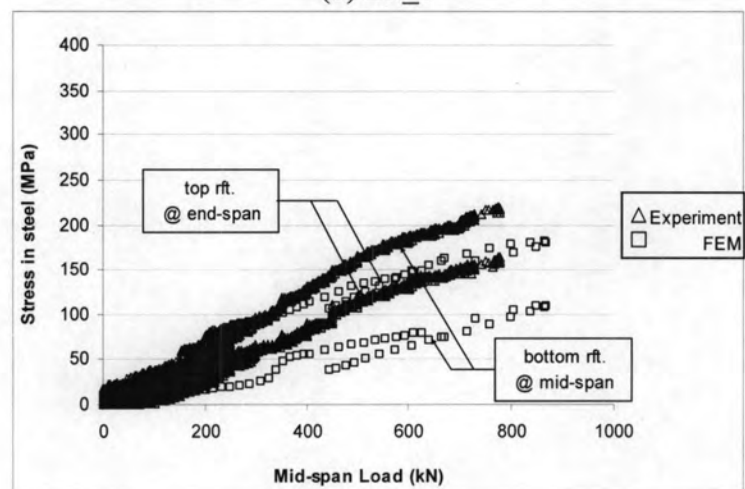
Fig. 4.1 Test set-up



(a) LS_H

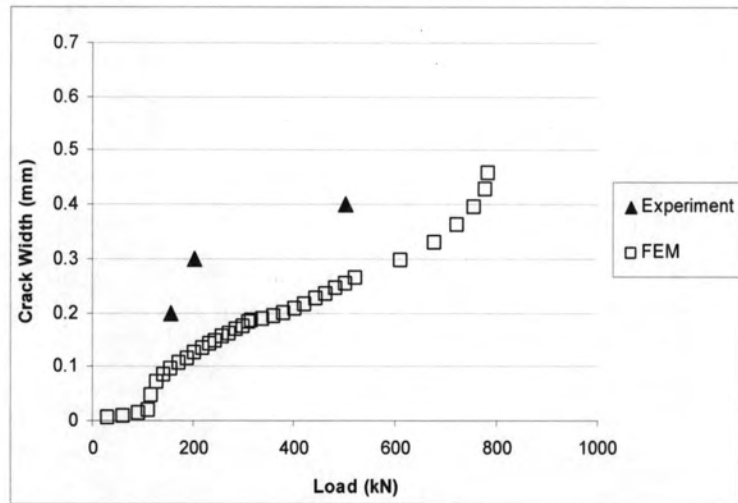


(b) LS_S

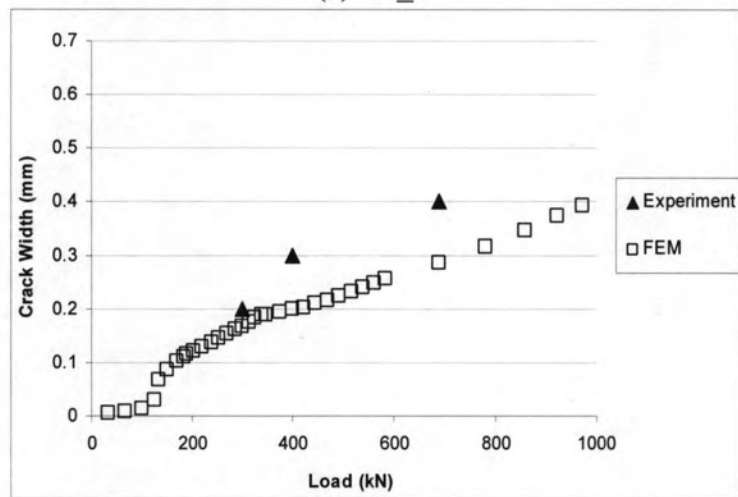


(c) LS_F

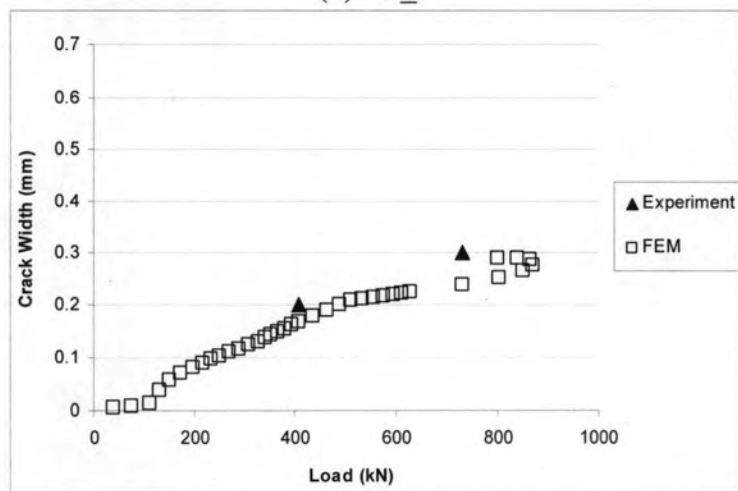
Fig. 4.2 Tensile stress in reinforcing steel comparison of FE analysis to experimental



(a) LS_H

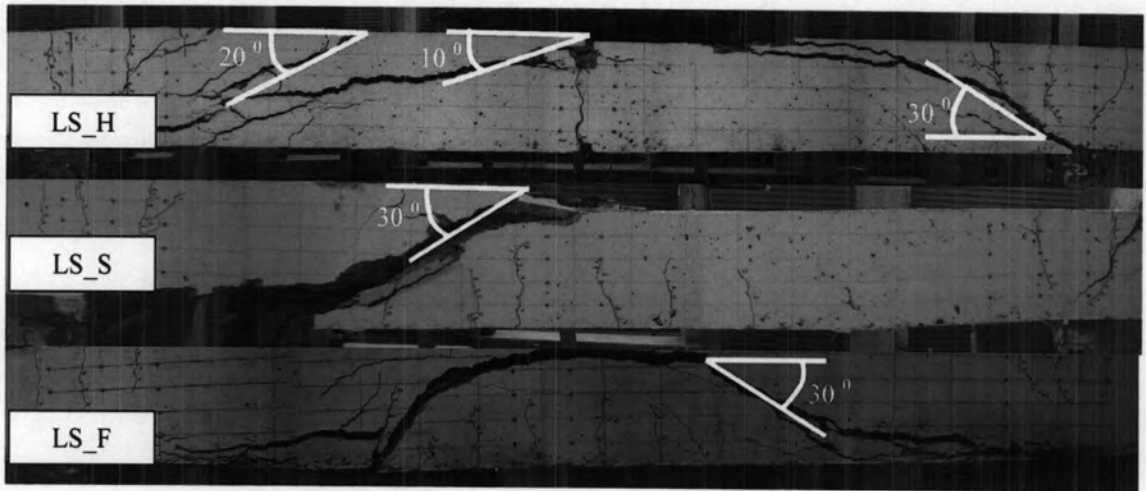


(b) LS_S

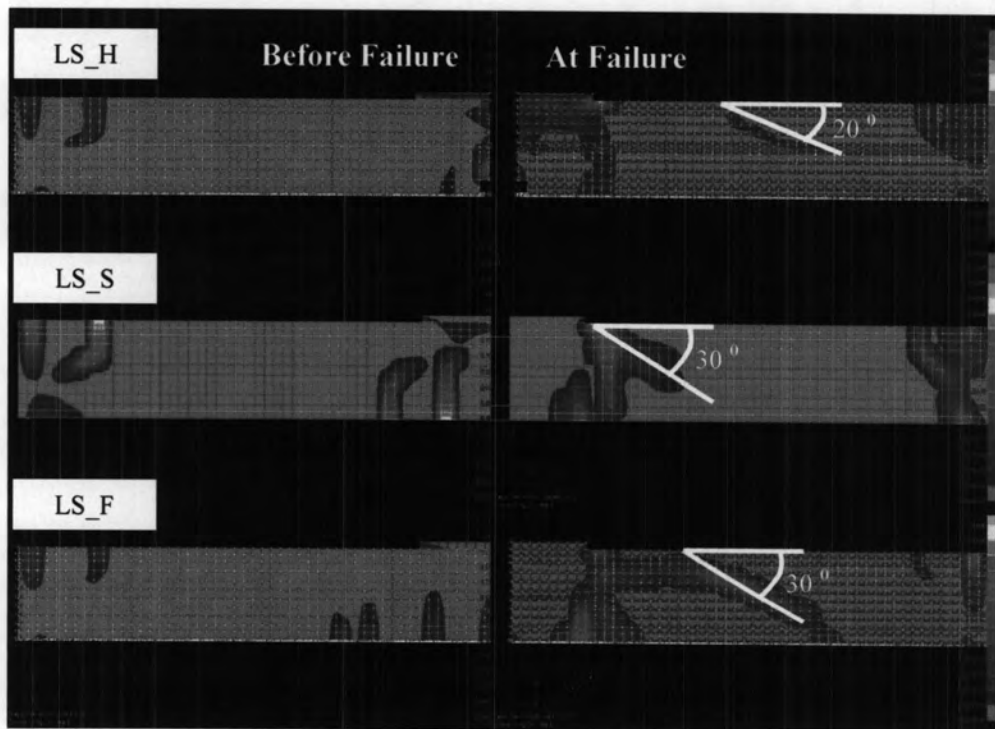


(c) LS_F

Fig. 4.3 Maximum crack width comparison of FE analysis to experimental



(a) Experimental



(b) FE analysis

Fig. 4.4 Crack pattern and mode of failure

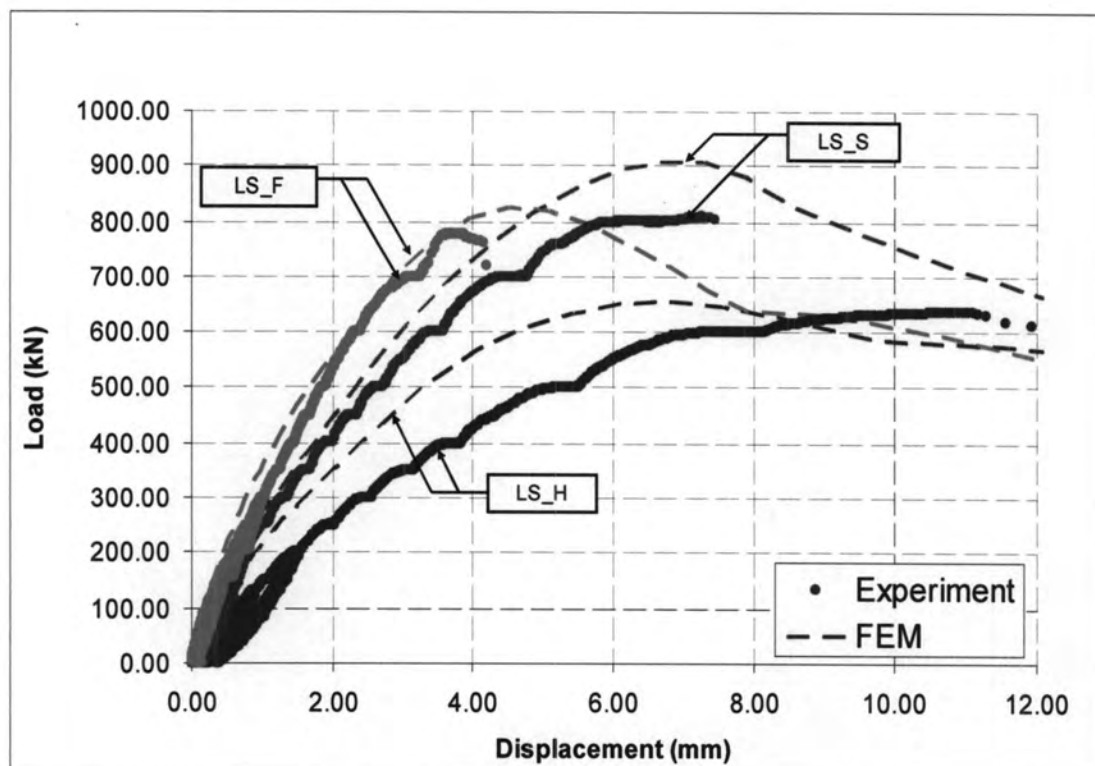
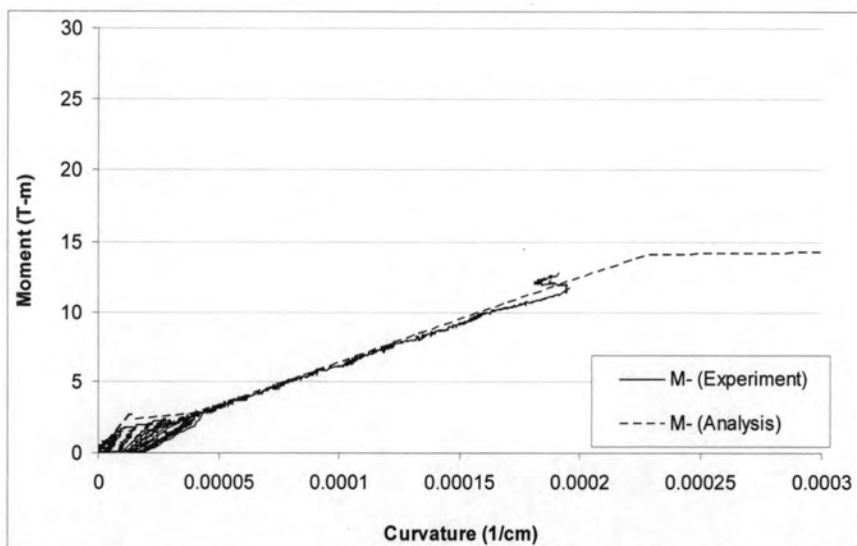
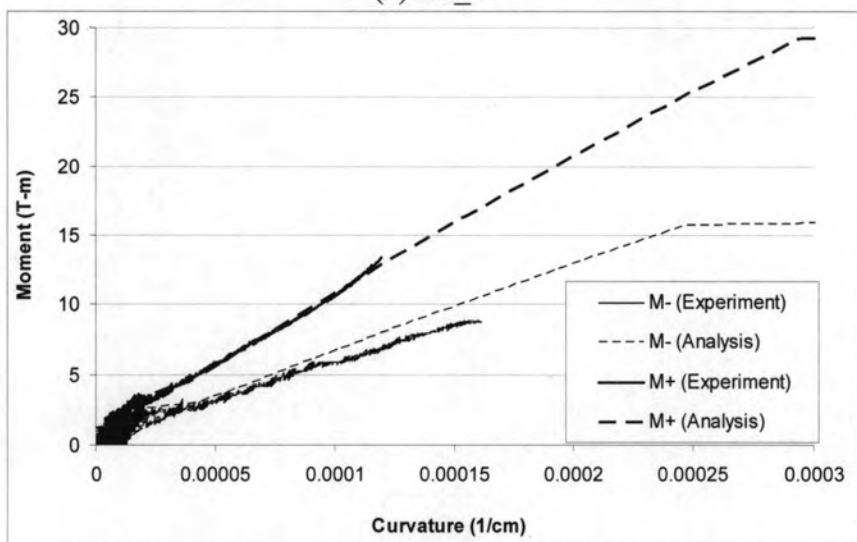


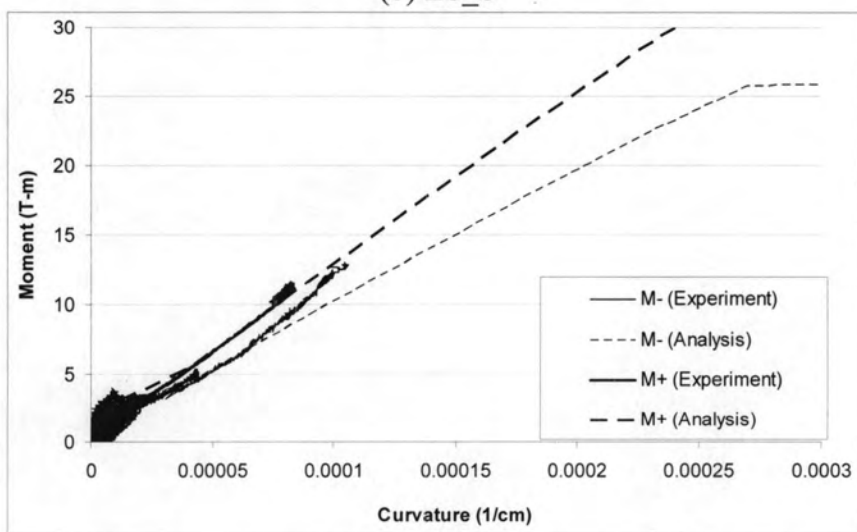
Fig. 4.5 Load and mid-span displacement comparison of FE analysis to experimental



(a) LS_H

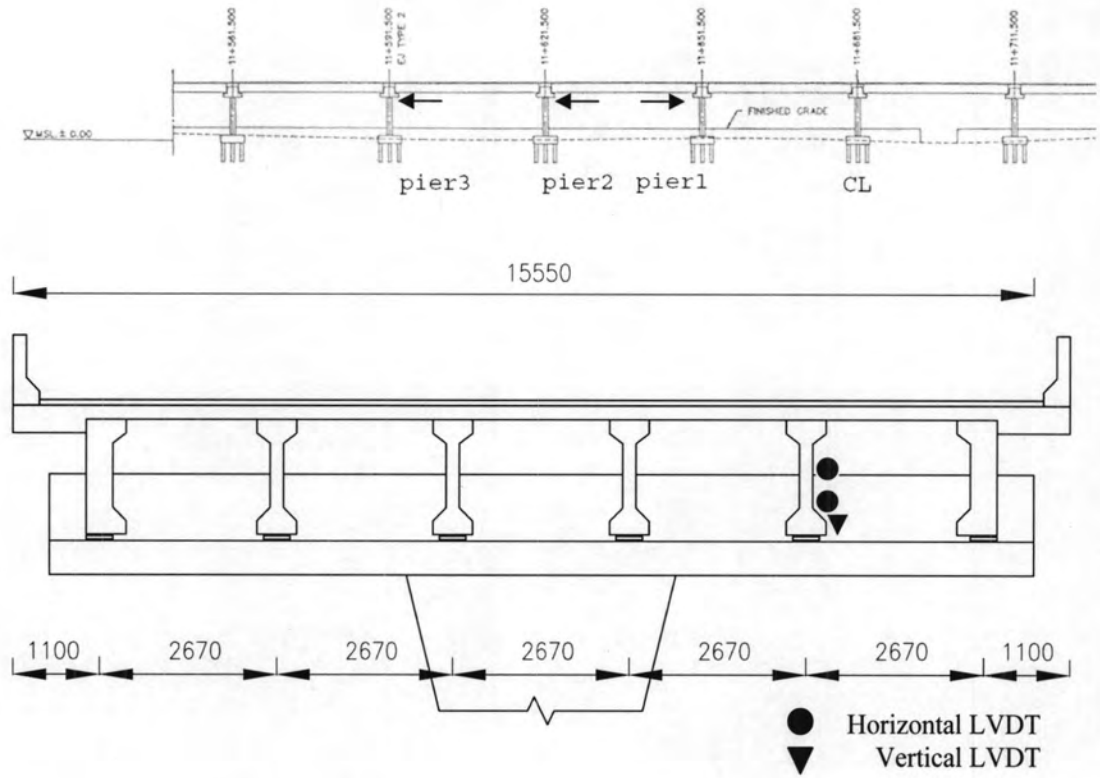


(b) LS_S

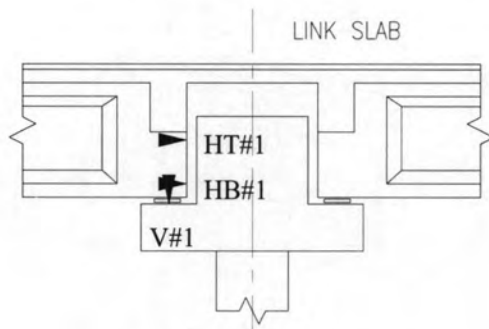


(c) LS_F

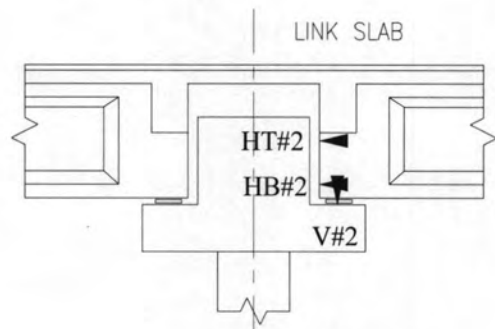
Fig. 4.6 Moment-curvature relationship comparison of FE analysis to experimental



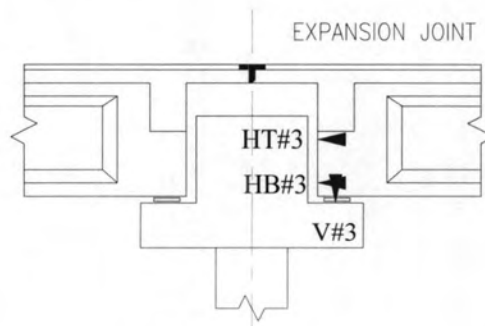
(a) Sectional elevation, typical cross-section (units in mm) and LVDT position



(b) Pier 1 set-up



(c) Pier 2 set-up



(d) Pier 3 set-up

Fig. 4.7 Schematic of on-site monitoring and instrument setting-up



(a) Structural system

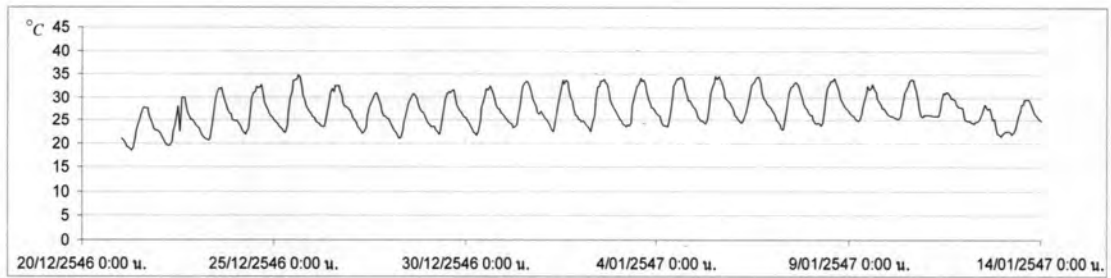
(b) End girder set-up



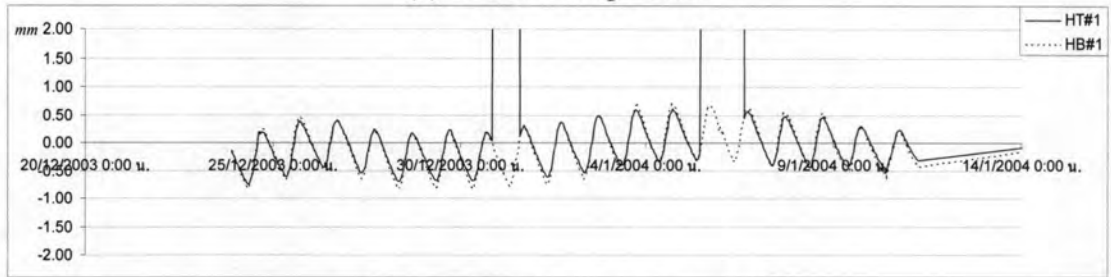
(c) End girder set-up (Alt.)

(d) Data acquisition system

Fig. 4.8 On-site monitoring and instrument setting-up



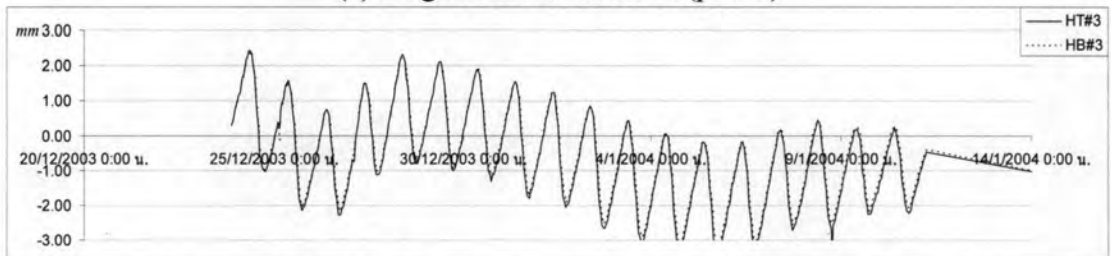
(a) ambient temperature



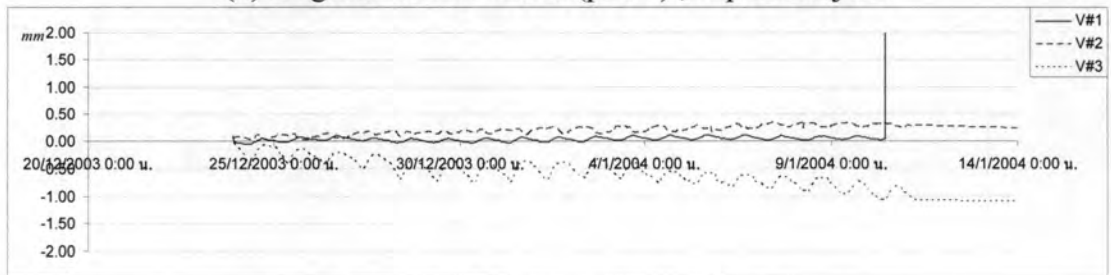
(b) longitudinal movement (pier 1)



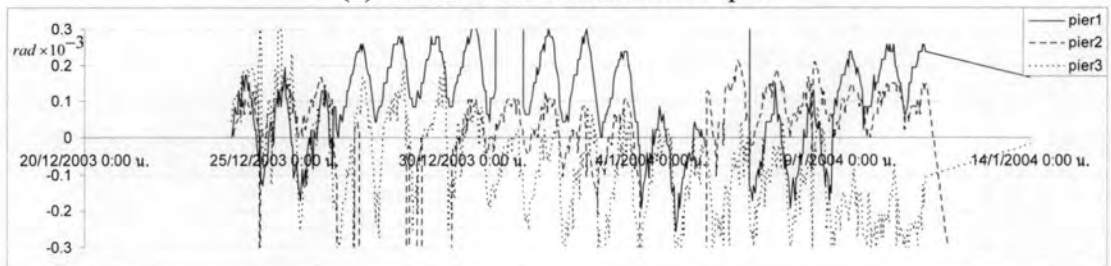
(c) longitudinal movement (pier 2)



(d) longitudinal movement (pier 3) ; expansion joint



(e) vertical movement at each pier



(f) End rotation at each pier

Fig. 4.9 On-site monitoring records (note that there are some losses of signal)